The comet-like composition of a protoplanetary disk as revealed by complex cyanides

Citation

Published Version

Permanent link

Terms of Use

Share Your Story

The cometary composition of a protoplanetary disk as revealed by complex cyanides[*]

Karin I. Öberg[1], Viviana V. Guzmán[1], Kenji Furuya[2], Chunhua Qi[1], Yuri Aikawa[3], Sean M. Andrews[1], Ryan Loomis[1], David J. Wilner[1]

May 26, 2015

[1]Harvard-Smithsonian Center for Astrophysics, 60 Garden Street, Cambridge, MA 02138, USA. [2]Leiden Observatory, Leiden University, P.O. Box 9513, 2300 CA Leiden, the Netherlands. [3]Kobe University, 1-1 Rokkodaicho, Nada Ward, Kobe, Hyogo Prefecture 657-0013, Japan.

Abstract

Observations of comets and asteroids show that the Solar Nebula that spawned our planetary system was rich in water and organic molecules. Bombardment brought these organics to the young Earth's surface, seeding its early chemistry[1]. Unlike asteroids, comets preserve a nearly pristine record of the Solar Nebula composition. The presence of cyanides in comets, including 0.01% of methyl cyanide (CH_3CN) with respect to water, is of special interest because of the importance of C-N bonds for abiotic amino acid synthesis[2]. Comet-like compositions of simple and complex volatiles are found in protostars, and can be readily explained by a combination of gas-phase chemistry to form e.g. HCN and an active ice-phase chemistry on grain surfaces that advances complexity[3]. Simple volatiles, including water and HCN, have been detected previously in Solar Nebula analogues – protoplanetary disks around young stars – indicating that they survive disk formation or are reformed *in situ*[4, 5, 6, 7]. It has been hitherto unclear whether the same holds for more complex organic molecules outside of the Solar Nebula, since recent observations show a dramatic change in the chemistry at the boundary between nascent envelopes and young disks due to accretion shocks[8]. Here we report the detection of CH_3CN (and HCN and HC_3N) in the protoplanetary disk around the young star MWC 480. We find abundance ratios of these N-bearing organics in the gas-phase similar to comets, which suggests an even higher relative abundance of complex cyanides in the disk ice. This implies that complex organics accompany simpler volatiles in protoplanetary disks, and that the rich organic chemistry of the Solar Nebula was not unique.

1

MWC 480 is a Herbig Ae star with an estimated stellar mass of 1.8 Solar masses ($M_\odot$) [9] in the Taurus star forming region at a distance of 140 pc. The star is surrounded by a 0.18±0.1 $M_\odot$ protoplanetary disk, an order of magnitude more massive disk than the Minimum Mass Solar Nebula[10, 11]. Compared to disks around Solar-type stars, the MWC 480 disk is 2–3 times warmer at a given radius[12, 13] and exposed to orders of magnitude higher ultraviolet radiation levels. Despite these environmental differences the volatile composition in the MWC 480 disk appears largely similar to that of disks around Solar-type stars, except for lower abundance of cold (T<20 K) chemistry tracers in the outer disk [14, 15]. The inner disk chemistry of MWC 480 has not been studied, but Herbig Ae and T Tauri disks are observed to present different volatile compositions close to their stars[16].

Using the Atacama Large Millimeter/submillimeter Array (ALMA), we detected two emission lines of CH_3CN from the MWC 480 protoplanetary disk (the $14_0 - 13_0$ line at 5σ, and the $14_1 - 13_1$ line at 3.5σ). We also detected emission lines from the N-bearing carbon chain HC_3N, and from the 13-C isotopologue of HCN. We targeted the 13-C isotopologue rather than the more abundant $H^{12}CN$ because the latter is optically thick and therefore a poor tracer of the HCN abundance. Figure 1 shows the spatially resolved line detections together with a dust continuum emission map, demonstrating the spatial coincidence between CH_3CN, HC_3N, HCN and dust emission from the disk. The angular resolution is 0."4 − 0".6, corresponding to 50–70 AU (1 AU is the distance from the Earth to the Sun). The emission is also spectrally resolved, which can be used to probe smaller spatial scales. Figure 1 shows the velocity gradient across the disk that arises from Keplerian rotation in all three lines. Figure 2 shows the spectra of the three lines; each displays the double-peaked structure typical of a rotating disk. Table 1 lists the integrated line fluxes.

We use the spectrally and spatially resolved line emission to constrain the radial profiles of molecular column density based on parametric abundance models defined with respect to the adopted MWC 480 disk density and temperature structure (Methods). Figures 2 and 3a-c show the synthetic line spectra and maps from the best-fit models, demonstrating the good match between the models and data. Figures 3d-f shows the best-fit radial column density profile, together with all profiles consistent with the data within 3σ, and abundances at 30 and 100 AU are reported in Table 1. The best-fit profiles have different slopes for the different molecules. The $H^{13}CN$ column density decreases with radius, which is consistent with predictions from disk chemistry models[17]. The increasing column density with radius of HC_3N, effectively a ring, is not predicted by models[18], indicative of that disk chemistry models are incomplete for HC_3N. The CH_3CN emission is best reproduced with a flat profile, but other profiles cannot be excluded.

The absolute abundances depend on the assumed disk density structure, and we therefore compare the complex cyanides in the MWC 480 disk to comet and to protostellar compositions using HCN as a reference species, similar to the practice in cometary studies[19]. We calculate abundances of CH_3CN and HC_3N with respect to HCN at 30 AU, the smallest disk radius accessible by the ALMA observations, and at 100 AU, the outer boundary of

the cyanide emission maps. Accounting for the higher luminosity of MWC 480 compared to the young Sun, this radial range in the MWC 480 disk corresponds to the comet forming zone of 10–30 AU in the Solar Nebula[19]. Assuming a standard $HCN/H^{13}CN$ ratio of 70, the best-fit HC_3N and CH_3CN abundances with respect to HCN are 0.4 and 0.05 at 30 AU, and 5 and 0.2 at 100 AU, respectively. The CH_3CN/HCN abundance ratios are robust to model assumptions to within factors of a few, while the HC_3N/HCN abundance ratio may be overestimated by an order of magnitude using our simple abundance model (Methods). Conservatively, both the CH_3CN and HC_3N abundances with respect to HCN are thus $\sim$5% at 30 AU and $\sim$20% at 100 AU. A typical comet contains 10% of CH_3CN and HC_3N with respect to HCN[19]. The MWC 480 gas-phase cyanide composition at both 30 and 100 AU is thus cometary within the observational and model uncertainties.

The relationship between gas-phase abundance ratios and the abundance ratios in ices, the main volatile reservoirs in disks[20, 17, 18], depends on both desorption characteristics and chemistry (Methods). HCN, HC_3N and CH_3CN are characterized by similar freeze-out and desorption kinetics, but different chemical pathways. In particular, the existence of efficient grain surface formation pathways to CH_3CN enhances CH_3CN with respect to the other cyanides in the ice mantles. The scale of this enhancement factor varies among models, but it is at least one order of magnitude (Methods). This results in an expected minimum CH_3CN/HCN ice ratio of 0.5 at 30 AU in the MWC 480 disk, considerably higher than the typical Solar System comet.

The CH_3CN/HCN and HC_3N/HCN ratios in the MWC 480 disk are also high when compared to protostars. The $HCN/HC_3N/CH_3CN$ ratio is 1/0.01/0.08 toward the Solar-type protostellar binary IRAS 16298-2422[21], and similar abundance ratios are found toward more massive systems. The MWC 480 cyanide composition is thus difficult to explain by inheritance alone, as has been suggested for e.g. H_2O[7]. Rather the observed high disk abundances likely reflect an efficient disk chemistry that readily converts a large portion of the carbon originally in CO and other small molecules into more complex organics[22, 23] during the first million years of the disk life time.

This early, efficient complex chemistry in protoplanetary disks impacts the surface conditions of rocky (exo-)planets. In the Grand Tack model of early Solar System dynamics[24], the coupled migration of Jupiter and Saturn in the gas-rich disk from which they formed caused scattering of volatile-rich (and thus complex organic-rich) planetesimals inwards, mixing with the asteroid belt, and outwards, producing the present-day Kuiper belt and comets[25]. While comets are expected (and observed) to conserve most of their original compositions due to low temperatures and thus very long desorption and chemical time scales[19], asteroid belt bodies are more processed. A combination of evaporation and chemistry probably resulted in both a net loss of volatiles and in a relative enhancement of complex organics with respect to H_2O over the subsequent 10s of Myr[26]. A second instability 100 million years later resulted in a heavy bombardment of the Earth by mainly asteroid belt bodies, including the icy bodies originating in the outer Solar System[27]. The frequency of these instabilities in exo-planetary systems is unknown, but the pile-up

3

of Hot Jupiters and Super-Earths reveal that major planetary migrations are common. When these migrations cause bombardment of icy bodies, they are likely organic-rich.

The high ratio of complex to simple cyanides in the MWC 480 disk implies that the rich organic composition of comets is not unique to our Solar System, and could be commonplace. Laboratory experiments have shown that the same ice chemistry that produce CH_3CN, i.e. photo processing of interstellar ice analogs also produce simple sugars and amino acids[28, 29]. This suggests that the early surface conditions of Earth, set by comet and asteroid bombardment, may be common for young rocky planets, and that conditions favourable to an even richer chemistry may be ubiquitous.

References

[1] Hartogh, P. *et al.* Ocean-like water in the Jupiter-family comet 103P/Hartley 2. *Nature* **478**, 218–220 (2011).

[2] Goldman, N., Reed, E. J., Fried, L. E., William Kuo, I.-F. & Maiti, A. Synthesis of glycine-containing complexes in impacts of comets on early Earth. *Nature Chemistry* **2**, 949–954 (2010).

[3] Herbst, E. & van Dishoeck, E. F. Complex Organic Interstellar Molecules. *ARAstron. Astrophys.* **47**, 427–480 (2009).

[4] Dutrey, A., Guilloteau, S. & Guelin, M. Chemistry of protosolar-like nebulae: The molecular content of the DM Tau and GG Tau disks. *Astron. Astrophys.* **317**, L55–L58 (1997).

[5] Carr, J. S. & Najita, J. R. Organic Molecules and Water in the Planet Formation Region of Young Circumstellar Disks. *Science* **319**, 1504–1506 (2008).

[6] Hogerheijde, M. R. *et al.* Detection of the Water Reservoir in a Forming Planetary System. *Science* **334**, 338–340 (2011).

[7] Cleeves, L. I. *et al.* The ancient heritage of water ice in the solar system. *Science* **345**, 1590–1593 (2014).

[8] Sakai, N. *et al.* Change in the chemical composition of infalling gas forming a disk around a protostar. *Nature* **507**, 78–80 (2014).

[9] Simon, M., Dutrey, A. & Guilloteau, S. Dynamical Masses of T Tauri Stars and Calibration of Pre-Main-Sequence Evolution. *Astrophys. J.* **545**, 1034–1043 (2000).

[10] Guilloteau, S., Dutrey, A., Piétu, V. & Boehler, Y. A dual-frequency sub-arcsecond study of proto-planetary disks at mm wavelengths: first evidence for radial variations of the dust properties. *Astron. Astrophys.* **529**, A105 (2011).

[11] Takami, M. *et al.* Surface Geometry of Protoplanetary Disks Inferred From Near-Infrared Imaging Polarimetry. *Astrophys. J.* **795**, 71 (2014).

[12] Chiang, E. I. & Goldreich, P. Spectral Energy Distributions of T Tauri Stars with Passive Circumstellar Disks. *Astrophys. J.* **490**, 368–376 (1997).

[13] D'Alessio, P., Calvet, N., Hartmann, L., Muzerolle, J. & Sitko, M. Models of Accretion Disks Around Young Stars. In Burton, M. G., Jayawardhana, R. & Bourke, T. L. (eds.) *Star Formation at High Angular Resolution*, vol. 221 of *IAU Symposium*, 403–410 (2004).

[14] Dutrey, A. *et al.* Chemistry in disks. I. Deep search for N_2H^+ in the protoplanetary disks around LkCa 15, MWC 480, and DM Tauri. *Astron. Astrophys.* **464**, 615–623 (2007).

[15] Öberg, K. I. *et al.* The Disk Imaging Survey of Chemistry with SMA. I. Taurus Protoplanetary Disk Data. *Astrophys. J.* **720**, 480–493 (2010).

[16] Pontoppidan, K. M. *et al.* A Spitzer Survey of Mid-infrared Molecular Emission from Protoplanetary Disks. I. Detection Rates. *Astrophys. J.* **720**, 887–903 (2010).

[17] Walsh, C., Millar, T. J. & Nomura, H. Chemical Processes in Protoplanetary Disks. *Astrophys. J.* **722**, 1607–1623 (2010).

[18] Walsh, C. *et al.* Complex organic molecules in protoplanetary disks. *Astron. Astrophys.* **563**, A33 (2014).

[19] Mumma, M. J. & Charnley, S. B. The Chemical Composition of Comets: Emerging Taxonomies and Natal Heritage. *ARAstron. Astrophys.* **49**, 471–524 (2011).

[20] Semenov, D. & Wiebe, D. Chemical Evolution of Turbulent Protoplanetary Disks and the Solar Nebula. *Astrophys. J.s* **196**, 25 (2011).

[21] van Dishoeck, E. F., Blake, G. A., Jansen, D. J. & Groesbeck, T. D. Molecular Abundances and Low-Mass Star Formation. II. Organic and Deuterated Species toward IRAS 16293-2422. *Astrophys. J.* **447**, 760–782 (1995).

[22] Ciesla, F. J. & Sandford, S. A. Organic Synthesis via Irradiation and Warming of Ice Grains in the Solar Nebula. *Science* **336**, 452–454 (2012).

[23] Favre, C., Cleeves, L. I., Bergin, E. A., Qi, C. & Blake, G. A. A Significantly Low CO Abundance toward the TW Hya Protoplanetary Disk: A Path to Active Carbon Chemistry? *Astrophys. J.L* **776**, L38 (2013).

[24] Tsiganis, K., Gomes, R., Morbidelli, A. & Levison, H. F. Origin of the orbital architecture of the giant planets of the Solar System. *Nature* **435**, 459–461 (2005).

[25] Walsh, K. J., Morbidelli, A., Raymond, S. N., O'Brien, D. P. & Mandell, A. M. A low mass for Mars from Jupiter's early gas-driven migration. *Nature* **475**, 206–209 (2011).

[26] Pizzarello, S. Catalytic syntheses of amino acids and their significance for nebular and planetary chemistry. *Meteoritics and Planetary Science* **47**, 1291–1296 (2012).

[27] O'Brien, D. P., Walsh, K. J., Morbidelli, A., Raymond, S. N. & Mandell, A. M. Water delivery and giant impacts in the Grand Tack scenario. *Icarus* **239**, 74–84 (2014).

[28] Öberg, K. I., Garrod, R. T., van Dishoeck, E. F. & Linnartz, H. Formation rates of complex organics in UV irradiated CH_3OH-rich ices. I. Experiments. *Astron. Astrophys.* **504**, 891–913 (2009).

[29] Muñoz Caro, G. M. *et al.* Amino acids from ultraviolet irradiation of interstellar ice analogues. *Nature* **416**, 403–406 (2002).

Addendum

Competing Interests The authors declare that they have no competing financial interests.

Author contributions K.I.Ö led the overall project, reduced the data, assisted by V.V.G. and R.L., and wrote the manuscript with revisions from S.M.A. and D.J.W. V.V.G., assisted by C.Q., performed the parametric modelling and abundance extraction. K.F. performed the astrochemical modelling, and interpreted the results with Y.A. All authors contributed to discussions of the results and commented on the manuscript.

Author information Correspondence and requests for materials should be addressed to K.I.Ö. (email: koberg@cfa.harvard.edu). The ALMA program number for the presented data is 2013.1.00226.

Table 1: Molecular data.

Molecule	QN	Rest freq.	E_u	Integrated flux [rms]	x^a_{30AU}	x^a_{100AU}
		GHz	K	mJy km/s beam^{-1}	$(10^{-13}\ n_H^{-1})$	$(10^{-13}\ n_H^{-1})$
H^{13}CN	J=3–2	259.0118	24.9	47[8]	1.6 [1.3–2.0]	1.6 [1.3–2.0]
HC$_3$N	J=27–26	245.6063	165	66[8]	43 [36–54]	480 [400–600]
CH$_3$CN	$14_0 - 13_0$	257.5274	92.7	30[6]	4.8 [2.3–7.5]	16 [6–55]
CH$_3$CN	$14_1 - 13_1$	257.5224	100	23[6]		

[a]best-fit abundances assuming a vertically constant abundance. the 3σ abundance range is in [].
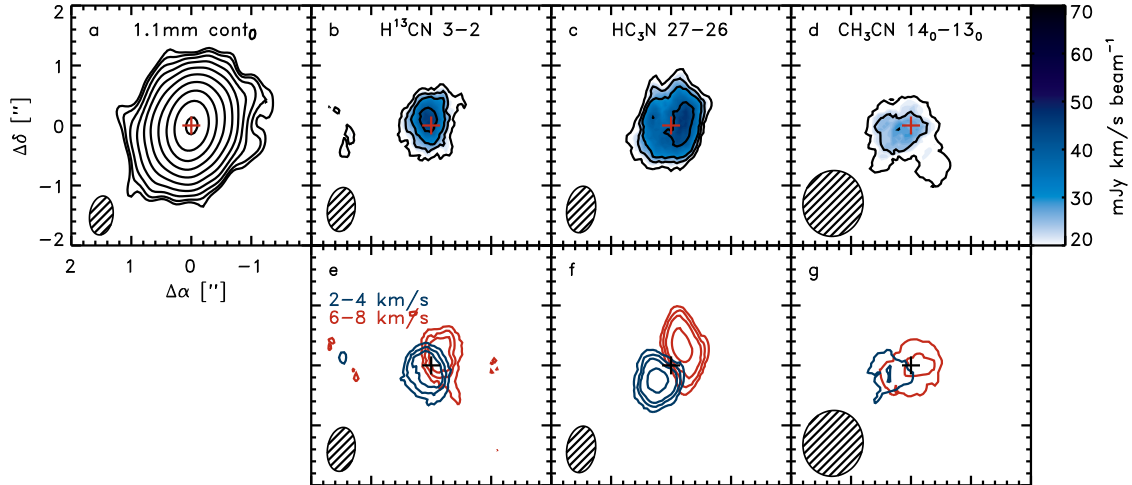

Figure 1: ALMA detections of simple and complex cyanides in the MWC 480 protoplanetary disk. a, 1.1 mm emission (black contours are $3\sigma + \sigma \times 2^{[1,2,...]}$). b–d, integrated emission of H^{13}CN (a), HC$_3$N (b) and CH$_3$CN (c) lines (colour: see colour scale on the right). Black contours are $[3,4,5,7,10]\sigma$. e–g, as b–d, but for 2 km/s velocity bins around the source mean velocity, displaying the disk rotation. Positions are relative to the continuum phase centre (marked with a cross) at right ascension (RA) 04:58:45.94 and declination (DEC) +29:50:38.4. The synthesized beam is shown in the bottom left corner of each panel.
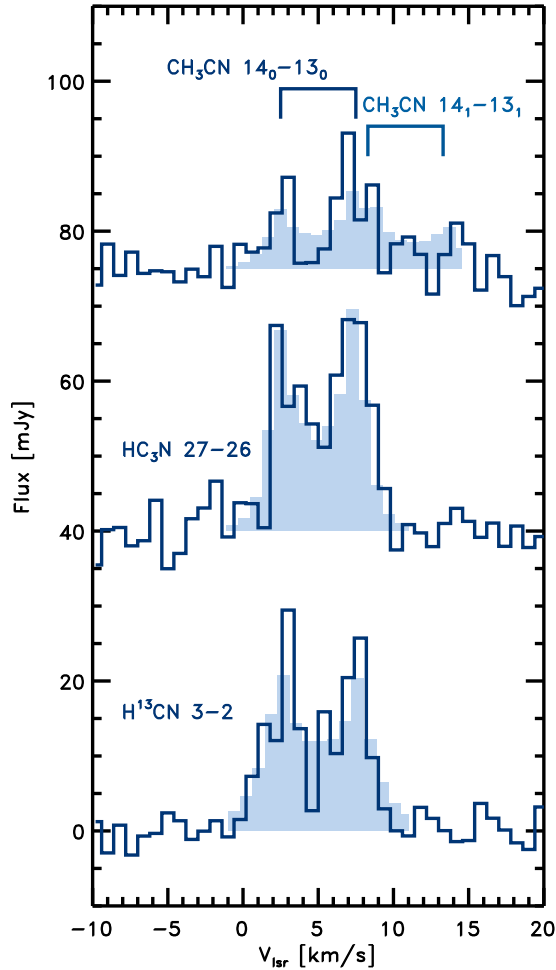
Figure 2: Spectra of detected cyanides in the MWC 480 protoplanetary disk. The observed spectra (contours) of $H^{13}CN$, HC_3N, and CH_3CN are extracted from ALMA spectral-image data cubes. The synthetic spectra (histograms) are based on the best fit disk abundance models in Fig. 3. The CH_3CN spectrum contains two partially overlapping lines identified with the $14_0 - 13_0$ and $14_1 - 13_1$ transitions. The spectra were extracted from the spectral image cubes using a Keplerian mask to maximize the signal-to-noise.
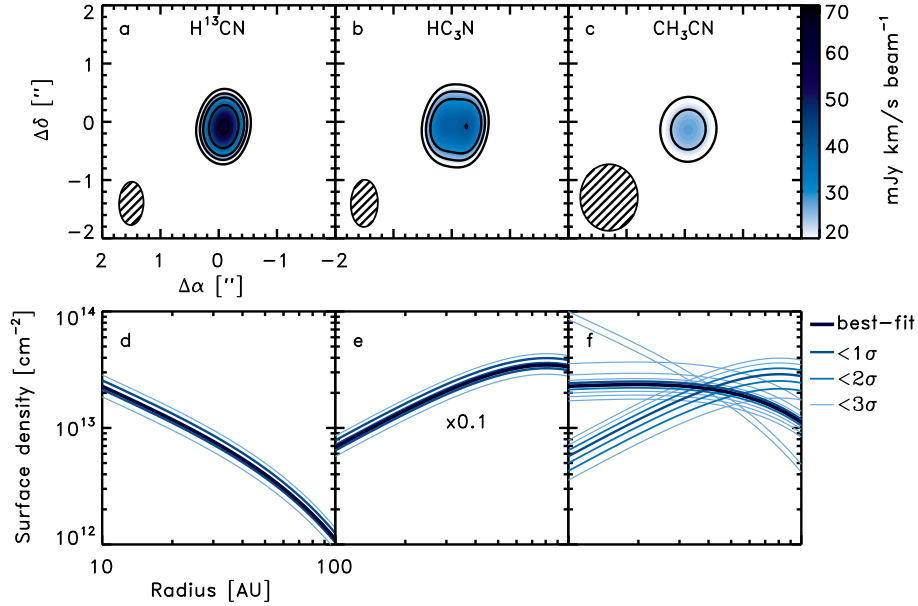
Figure 3: Models of cyanide emission and radial distributions in the MWC 480 disk. a-c, synthetic ALMA observations without added noise based on the best-fit radial column density profiles of $H^{13}CN$, HC_3N, and CH_3CN (colour: see colour scale on the right). Black contours are as in Fig. 1. d-e, best-fit radial column density profiles (thick dark blue line), shown together with all column density profiles that are consistent with data within 1, 2 and 3σ confidence intervals. Increasing deviations from the best-fit are shown with successively lighter shades and thinner lines.

Methods

ALMA observations and data reduction.

MWC 480 was observed with the Atacama Large Millimeter/submillimeter Array as a part of the Cycle 2 proposal 2013.1.00226. Observations were carried out on 2014 June 15, with 33 antennas and baselines of 18–650 m (15–555 kλ). The total on source integration time was 22 minutes. The nearby quasar J0510+1800 was used for phase and gain, bandpass and absolute flux calibration (J0510+1800 was itself calibrated to an absolute flux of 1.50[0.08] Jy on 2014 June 29). The correlator was configured to observe 14 spectral windows (SPWs) with resolution $\delta\nu$= 61.04 kHz. The H^{13}CN 3–2 line was placed in SPW 1, HC$_3$N 27-26 in SPW 9 and CH$_3$CN 14_0-13_0 and 14_1-13_1 in SPW 5, each 60–120 MHz wide and centered on 258.983, 245.622 and 257.498 GHz, respectively.

The visibility data were calibrated by ALMA/ NAASC staff following standard procedures. Each SPW was further self-calibrated in phase and amplitude in CASA 4.2.2. The self-calibrated phase and gain SPW-specific solutions were applied to create individual SPW line data cubes using the Briggs weighting scheme, with Brigg's robustness parameter set to 1–2. For the weak CH$_3$CN lines, a taper of 1″ was applied to the visibilties to maximize the signal-to-noise. The data cubes were subsequently continuum subtracted using channels identified as free of spectral line emission. The resulting rms noise in 1 km/s bins was ∼2.3 mJy per beam. A CLEAN deconvolution was performed with a mask produced manually based on the H^{13}CN emission and applied to the HC$_3$N and CH$_3$CN spectral line cubes (after verifying that the HC$_3$N and CH$_3$CN cubes contained no additional emission). For the 257 GHz continuum map, obtained by combining all SPWs in the USB), the synthesized beam is 0.″65 × 0.″39 (PA=-7°) and rms noise 0.3 mJy beam^{-1}. The 257 GHz continuum flux density was determined to be 331±33 mJy (assuming a 10% uncertainty in the absolute calibration), which agrees well with previous Submillimer Array results[30].

Integrated emission maps were produced using the *immoments* task in CASA, adding emission >1σ from each channel. Lower clipping levels do not change the result at the 10% level. Spectra were extracted using both the empirical CLEAN masks and theoretical masks based on Keplerian rotation to isolate disk emission in each channel. The CLEAN masks resulted in the best signal-to-noise ratio, and these results are used in the study.

Parametric disk density and temperature model.

We adopt a previously developed disk density structure of MWC 480[10]. The total surface density is given by the similarity solution, which self-consistently describes the density structure of an accretion disk[31,32]:

$$\Sigma(r) = \Sigma_c \left(\frac{r}{R_c}\right)^{-\gamma} \exp\left(-\left(\frac{r}{R_c}\right)^{2-\gamma}\right), \tag{1}$$

where $\Sigma_c = M_{gas}(2 - \gamma)/(2\pi R_c^2)$ is a normalization coefficient, R_c is the characteristic radius, and γ is a gradient parameter describing the density fall-off with radius. The two-dimensional density structure in cylindrical coordinates is

$$\rho(r,z) = \frac{\Sigma(r)}{H(r)\pi} \exp\left(\frac{-z^2}{H(r)^2}\right), \tag{2}$$

where $H(r) = H_{100}(r/100AU)^h$ is the scale height, and h a parameter that describes the amount of flaring of the disk. The density structure parameters were constrained using high angular resolution observations of the MWC 480 dust continuum emission at 1.3 mm and 3 mm wavelengths [10] and are listed in Extended Data Table 1. The resulting mass surface densities in g cm^{-2} are 550, 91 and 4.7 at 1, 10 and 100 AU, respectively.

Based on existing model fits to dust and ^{13}CO observations[33,34], the disk midplane temperature is parametrized as $T(r) = T_0 \left(\frac{r}{R_0}\right)^{-q}$, where T_0 is set to 23 K at $R_0 = 100$ AU, and the power-law index q is 0.4. To account for the presence of a vertical temperature gradient due to heating of the disk surface by the central star[34,35], we parameterize the two-dimensional temperature structure in cylindrical coordinates as

$$T(r,z) = T_0 \left(\frac{r}{R_0}\right)^{-q} \exp\left(\log\beta\frac{z}{H(r)}\right), \tag{3}$$

where T_0 is the midplane temperature at R_0, q is a power-law index describing the decrease in midplane temperature with radius, and β is a factor describing the increase in temperature at increasing disk height, which is set to 1.5[34]. The density and temperature disk structures are shown in Extended Data Fig. 1.

Molecular abundance retrieval.

To retrieve molecular abundance and column density profiles, we define parametric abundance models with respect to the adopted MWC 480 disk density and temperature structure. We use a simple power-law prescription $x = x_{100AU} \times (r/100\ AU)^\alpha$ for the molecular abundances where x is the abundance of the molecule with respect to the total hydrogen density, x_{100AU} is the abundance at 100 AU, r is the disk radius in AU, and α is a power law index[36]. To obtain a column density profile, which is more intuitively related to observations, the abundance prescription is multiplied by disk surface density profile, Eq. 1. We set an outer cut-off radius of 100 AU, corresponding to the most extended emission observed for any of the cyanides. We also explored R_{out} of 60 and 80 AU, but this did not improve the fit for any of the molecules. For each molecule, we calculate a grid of abundance models that covers x_{100AU} from $10^{-14} - 10^{-10}$ with respect to n_H, and α between 0 and 1 for H^{13}CN, 1 and 2 for HC$_3$N, 0 and 2 for CH$_3$CN. These initial ranges of α were selected based on visual inspection of the observed emission, noting its level of central

concentration, i.e. $\alpha = 0$ corresponds to a steeply decreasing column density profile, $\alpha = 1$ to an almost flat profile, and $\alpha = 2$ to an increasing profile with radius.

The best-fit models are obtained by minimizing χ^2, the weighted difference between the real and imaginary part of the complex visibility measured in the (u, v)-plane sampled by the ALMA observations[36,37,38]. We use the three-dimensional Monte Carlo code LIME[39] to calculate the radiative transfer and molecular excitation. In addition to the molecular abundance profile and the disk density and temperature structure parameters, the radiative transfer modelling requires information on disk inclination, turbulence and velocity field. We adopted a disk inclination of $37°$, disk turbulence of 0.05 km/s and a Keplerian velocity field with a stellar mass of 1.8 $M_\odot$[10]. For HCN and HC_3N, the level populations were computed in non-LTE (Local Thermodynamic Equilibrium) with collision rates listed in the BASECOL database[40,41]. For CH_3CN, we assumed LTE, which is a reasonable approximation, since the expected disk emissive layers have higher densities than the critical density. We checked this assumption by running several HCN and HC_3N models assuming LTE and found a good agreement (within 20%) between LTE and non-LTE models. In Extended Data Fig. 2 we show the best-fit models for different α. In the case of HC_3N, only the models with $\alpha = 2$ shows the observed ring-like structure and are therefore the only ones considered further.

Within the adopted model framework, the molecular abundances and abundance ratios are constrained within a factor of a few. These models implicitly assume a constant abundance profile with disk height, which may be a poor approximation in the outer disk where freeze-out in the midplane results in a vertically layered structure[20],[42,43]. The existing data are, however, insufficient to put any constraints on the vertical distribution. Rather than pursuing a more complex model, we opt to test the sensitivity of the derived abundances and abundance ratios on the details of the vertical structure assumptions. We ran a second grid of models to simulate the effect of freeze-out in the midplane by reducing the molecular abundances by three orders of magnitude at $z/R < 0.2$. Using the same fitting procedure as before, we find best-fit x_{100au} of 1×10^{-11} (α=0), 3.5×10^{-10} (α=2), and 5×10^{-11} (α=1), for $H^{13}CN$, HC_3N and CH_3CN, respectively. These abundances are an order of magnitude higher than those obtained assuming a vertically constant abundance. The $CH_3CN/H^{13}CN$ abundance ratio profile is unchanged within the model uncertainties, however. Despite a higher excitation level of CH_3CN the two molecules emit from a similar disk layer when assigned the same vertical abundance profile due to a combination of a high critical density of the CH_3CN transition and a rapid fall-off in density with disk height, i.e. practically no CH_3CN emission originates at $z/R > 0.5$. In contrast, the derived HC_3N/HCN ratio does depend on the vertical structure. The HC_3N transition has an even higher energy level and a lower critical density than CH_3CN, which implies that some of the HC_3N emission can originate in more elevated disk layers than $H^{13}CN$ and CH_3CN. The reported $CH_3CN/H^{13}CN$ results are thus robust to the abundance model assumptions, while the reported $HC_3N/H^{13}CN$ results may be overestimated by up to an order magnitude.

Disk chemistry modelling: constraining the ice-to-gas ratios.

To constrain the origin of CH_3CN and therefore how its ice-to-gas ratio compares with HCN, we first explore how much of the observed CH_3CN gas could come from gas-phase chemistry. We ran a grid of pseudo-time dependent models with a complete gas-phase chemistry[44], but without any grain surface reactions (except for adsorption and desorption, and H_2 formation on grains), for 1 Myr. The grid covers several orders of magnitude of densities, temperatures, UV fields and ionization fractions – the four most important regulators of gas-phase chemistry in disks. For gas-phase CH_3CN production, the ionization rate is expected to be of special importance because the main gas-phase formation pathway includes CH_3^+ (through $HCN+CH_3^+$, which has a expert-validated reaction rate in the KIDA database[45]). Extended Data Figure 3 shows that none of these models can produce $CH_3CN/HCN > 0.01$ and that in the vast majority of the parameter space $CH_3CN/HCN < 0.001$. A ratio of 0.01 is approached for an ionization rate of 10^{-14} s^{-1}, but such high ionization rates are only attained in the disk atmosphere where stellar X-rays regulate the ionization balance. This disk layer contain a very small fraction of the total disk mass and therefore contributes a negligible amount of the total molecular column. Deeper into the disk, the ionization rate is reduced below 10^{-17} s^{-1} because of attenuation of both X-rays and cosmic rays[46]. A ratio of 0.01 is also approached at lower ionization rates at very low temperatures and high densities. Such environments are characteristic for the outer disk midplane, which contain a lot of mass, but freeze-out at these temperatures results in CH_3CN abundances below 10^{-14}, which would not contribute to the observed CH_3CN emission. The observed high abundance of CH_3CN gas with respect to HCN therefore implies that grain surface chemistry contributes significantly to the observed CH_3CN abundance.

We ran a number of complete disk chemistry models for 1Myr, the estimated age of the MWC 480 star+disk system, which include gas and grain surface chemistry, as well as different levels of turbulence, to calculate the range of plausible ice-to-gas conversion factors for HCN (and other gas-phase chemistry products) and CH_3CN[47]. The main grain surface CH_3CN formation pathways in these models are hydrogenation of C_2N and CH_3+CN and ice photochemistry. The main desorption pathway is UV photodesorption because of the high binding energies of HCN. HC_3N and CH_3CN: 4170, 4580, and 4680 K, respectively[48,49,50], respectively, corresponding to sublimation temperatures of $\sim$90 K at a gas density of 10^6 cm^{-3} and 110 K at the gas density of 10^{10} cm^{-3}. The three cyanides should also present very similar UV photodesorption efficiencies because of similar radiation cross-sections and binding energies[51]. Absent grain surface chemistry, these molecules would thus have had comparable ice-to-gas ratios.

Because CH_3CN can form on the grains in the cold midplane a key feature is the coupling between the ice formation layer and the disk layers where molecules are efficiently desorbed into the gas-phase. Without such a coupling, ice chemistry cannot affect the gas-phase volatile composition. In the disk models, we define the vertical diffusion coefficient

13

as $D_z = \alpha_z c_s^2 / \Omega$, where α_z is a free parameter, c_s is the local sound velocity, and Ω is the Keplerian orbital frequency. Different levels of turbulence are simulated by different values of α_z between 0 and 0.01. In models with turbulence turned off ($\alpha_z = 0$), there is no mixing between the cold, icy midplane and the intermediate layers where gas-phase molecules are abundant (and the observed cyanides likely reside). Extended Data Figure 4a shows that without turbulence the predicted CH_3CN abundances are low everywhere ($< 10^{-11}$ w.r.t n_H, where n_H is the number density of H nuclei) and the vertically averaged CH_3CN/HCN abundance ratio is <0.001; see Extended Data Figure 5a,d).

In models that include vertical mixing ($\alpha_z = 0.001 - 0.01$), the CH_3CN abundance as well as the CH_3CN/HCN abundance ratio are enhanced by an order of magnitude because of mixing of midplane icy grains into UV exposed disk regions where the ices photodesorb (Extended Data Figs. 4 and 5). In particular the CH_3CN/HCN ratio approaches 10^{-2} outside of 30 AU, within an order of magnitude of the observed ratios. Model-data comparison thus suggest that the intermediate disk layers are strongly coupled to the icy midplane through mixing. This implies that gas-phase observations of CH_3CN and other cyanides at intermediate disk heights can be used to trace the total volatile reservoir, even if the conversion from gas to ice can be complex.

Using the three models, with no, moderate and strong mixing we calculate the HCN and CH_3CN ice-to-gas density and column density ratios as a function of disk radius (Extended Data Fig. 6,7). For HCN, the ice-to-gas ratio varies between 10^5 and 10^3 between 30 and 100 AU. For CH_3CN the ice-to-gas ratio varies between 10^7 and 10^4. In other disk chemistry models[18],[52] the contrast between the two ice-to-gas ratios is even higher. Considering the range of values and their sensitive dependence on assumptions about disk turbulence, we conclude that the ice-to-gas ratio for CH_3CN is at least 10 times higher than HCN and HC_3N. At longer time scales the balance between formation in the midplane and destruction at more exposed disk layers determines whether the CH_3CN abundance increases or decreases – in general the more turbulence the faster the destruction.

It is important to note, that we employ generic disk structures[53] that have not been fit to the MWC 480 data. The temperature and density structures are comparable (cf. Extended Data Figs. 1 and 4). The UV field is lower than would be expected toward a Herbig Ae star and the gas-phase CH_3CN production may therefore be somewhat overestimated in our model, but as shown above, gas-phase chemistry is a minor contributor to the overall CH_3CN gas budget. The grain surface production takes place in UV shielded regions and should thus not be affected by an increased UV flux. An increased UV field intensity may change the desorption/adsorption balance, however, since UV photodesorption is an important desorption mechanism. This increase in photodesorption will be accompanied by an increased level photodissociation and the main effect will therefore be to push the desorbing layer closer to the midplane rather than increasing its abundance. An A star type radiation field may aid the detection of gas-phase CH_3CN, since less turbulence may be required to bring the icy grains up to UV exposure and into the gas-phase. A decrease in the disk height of the cyanide gas layer, compared to our generic disk model, may

also reduce the absolute ice-to-gas ratios, but the relative ratios of species with similar adsorption and desorption characteristics should not be significantly affected.

Desorption Mechanism

In our disk chemistry model, UV photodesorption regulates the desorption of oh HCN, HC_3N and CH_3CN ice into the gas-phase. This result depends on a combination of disk and star properties and on the theoretical yields of different desorption mechanisms, many of which are poorly constrained. While relative ice-to-gas ratios of related species are insensitive to the details of the desorption process, the absolute ice-to-gas ratios found in our models must be considered highly uncertain. Based on theory, different desorption mechanisms should present different radial and vertical abundance distributions, which could be tested observationally. Desorption due to release of chemical formation energy should be most important in the cold disk midplane, while UV photodesorption is only efficient in warmer, upper disk layers, and thermal desorption in the disk layers that are warm enough. In particular, colder molecular emission layers should be characterized by lower excitation temperatures, which can be measured when multiple lines of the same species are observed. Observational constraints on ice desorption in disks will thus be attainable with ALMA.

Different desorption mechanisms should also exhibit different chemical signatures, although the details are often model-dependent. In the case of thermal desorption, the gas phase composition in a layer should simply depend on volatility, albeit with the added complication of ice entrapment[54]. Chemistry can also help distinguish between ice and gas origins and thus provide an independent measure of the relative importance of the two pathways. he high ratio of CH_3CN/CH_3NC in the Horsehead PDR (Photon Dominated Region), for example, was used as evidence for a grain surface origin of the observed CH_3CN[55]. Chemical tracers could also provide useful constraints on the incident radiation fields and temperature structure and thus aid in ruling out some of the potentially important desorption mechanisms. For example CN/HCN is a proposed tracer of UV flux and HNC/HCN of temperature[56,57].

30. Öberg, K. I. *et al.* Disk Imaging Survey of Chemistry with SMA. II. Southern Sky Protoplanetary Disk Data and Full Sample Statistics. *Astrophys. J.* **734**, 98 (2011).

31. Lynden-Bell, D. & Pringle, J. E. The evolution of viscous discs and the origin of the nebular variables. *Mon. Not. R. Astron. Soc.* **168**, 603–637 (1974).

32. Hartmann, L., Calvet, N., Gullbring, E. & D'Alessio, P. Accretion and the Evolution of T Tauri Disks. *Astrophys. J.* **495**, 385–400 (1998).

33. Piétu, V., Dutrey, A., Guilloteau, S., Chapillon, E. & Pety, J. Resolving the inner dust disks surrounding LkCa 15 and MWC 480 at mm wavelengths. *Astron.*

Astrophys. **460**, L43–L47 (2006).

34. Dartois, E., Dutrey, A. & Guilloteau, S. Structure of the DM Tau Outer Disk: Probing the vertical kinetic temperature gradient. *Astron. Astrophys.* **399**, 773–787 (2003).

35. Rosenfeld, K. A., Andrews, S. M., Wilner, D. J., Kastner, J. H. & McClure, M. K. The Structure of the Evolved Circumbinary Disk around V4046 Sgr. *Astrophys. J.* **775**, 136 (2013).

36. Qi, C. *et al.* Imaging of the CO Snow Line in a Solar Nebula Analog. *Science* **341**, 630–632 (2013).

37. Qi, C., Wilner, D. J., Aikawa, Y., Blake, G. A. & Hogerheijde, M. R. Resolving the Chemistry in the Disk of TW Hydrae. I. Deuterated Species. *Astrophys. J.* **681**, 1396–1407 (2008).

38. Qi, C. *et al.* Resolving the CO Snow Line in the Disk around HD 163296. *Astrophys. J.* **740**, 84 (2011).

39. Brinch, C. & Hogerheijde, M. R. LIME - a flexible, non-LTE line excitation and radiation transfer method for millimeter and far-infrared wavelengths. *Astron. Astrophys.* **523**, A25 (2010).

40. Wernli, M., Wiesenfeld, L., Faure, A. & Valiron, P. Rotational excitation of HC_3N by H_2 and He at low temperatures. *Astron. Astrophys.* **464**, 1147–1154 (2007).

41. Dubernet, M., Nenadovic, L. & Doronin, N. SPECTCOL: A New Software to Combine Spectroscopic Data and Collisional Data within VAMDC. In Ballester, P., Egret, D. & Lorente, N. P. F. (eds.) *Astronomical Data Analysis Software and Systems XXI*, vol. 461 of *Astronomical Society of the Pacific Conference Series*, 335–338 (2012).

42. Aikawa, Y. & Herbst, E. Molecular evolution in protoplanetary disks. Two-dimensional distributions and column densities of gaseous molecules. *Astron. Astrophys.* **351**, 233–246 (1999).

43. Walsh, C., Millar, T. J. & Nomura, H. Molecular Line Emission from a Protoplanetary Disk Irradiated Externally by a Nearby Massive Star. *Astrophys. J.L* **766**, L23 (2013).

44. Aikawa, Y., Wakelam, V., Hersant, F., Garrod, R. T. & Herbst, E. From Prestellar to Protostellar Cores. II. Time Dependence and Deuterium Fractionation. *Astrophys. J.* **760**, 40 (2012).

45. Wakelam, V. *et al.* A KInetic Database for Astrochemistry (KIDA). *Astrophys. J.S* **199**, 21 (2012).

46. Cleeves, L. I., Bergin, E. A., Qi, C., Adams, F. C. & Oberg, K. I. Constraining the X-ray and Cosmic Ray Ionization Chemistry of the TW Hya Protoplanetary Disk: Evidence for a Sub-interstellar Cosmic Ray Rate. *ArXiv e-prints* (2014).

47. Furuya, K. & Aikawa, Y. Reprocessing of Ices in Turbulent Protoplanetary Disks: Carbon and Nitrogen Chemistry. *Astrophys. J.* **790**, 97 (2014).

48. Yamamoto, T., Nakagawa, N. & Fukui, Y. The chemical composition and thermal history of the ice of a cometary nucleus. *Astron. Astrophys.* **122**, 171–176 (1983).

49. Garrod, R. T. & Herbst, E. Formation of methyl formate and other organic species in the warm-up phase of hot molecular cores. *Astron. Astrophys.* **457**, 927–936 (2006).

50. Collings, M. P. *et al.* A laboratory survey of the thermal desorption of astrophysically relevant molecules. *Mon. Not. R. Astron. Soc.* **354**, 1133–1140 (2004).

51. van Dishoeck, E. F., Jonkheid, B. & van Hemert, M. C. Photoprocesses in protoplanetary disks. *Faraday Discussions* **133**, 231–343 (2006).

52. Walsh, C., Nomura, H., Millar, T. J. & Aikawa, Y. Chemical Processes in Protoplanetary Disks. II. On the Importance of Photochemistry and X-Ray Ionization. *Astrophys. J.* **747**, 114 (2012).

53. Nomura, H., Aikawa, Y., Tsujimoto, M., Nakagawa, Y. & Millar, T. J. Molecular Hydrogen Emission from Protoplanetary Disks. II. Effects of X-Ray Irradiation and Dust Evolution. *Astrophys. J.* **661**, 334–353 (2007).

54. Fayolle, E. C., Öberg, K. I., Cuppen, H. M., Visser, R. & Linnartz, H. Laboratory $H_2O:CO_2$ ice desorption data: entrapment dependencies and its parameterization with an extended three-phase model. *Astron. Astrophys.* **529**, A74 (2011).

55. Gratier, P. *et al.* The IRAM-30 m line survey of the Horsehead PDR. III. High abundance of complex (iso-)nitrile molecules in UV-illuminated gas. *Astron. Astrophys.* **557**, A101 (2013).

56. Bergin, E., Calvet, N., D'Alessio, P. & Herczeg, G. J. The Effects of UV Continuum and Lyα Radiation on the Chemical Equilibrium of T Tauri Disks. *Astrophys. J.L* **591**, L159–L162 (2003).

57. Graninger, D. M., Herbst, E., Öberg, K. I. & Vasyunin, A. I. The HNC/HCN Ratio in Star-forming Regions. *Astrophys. J.* **787**, 74 (2014).
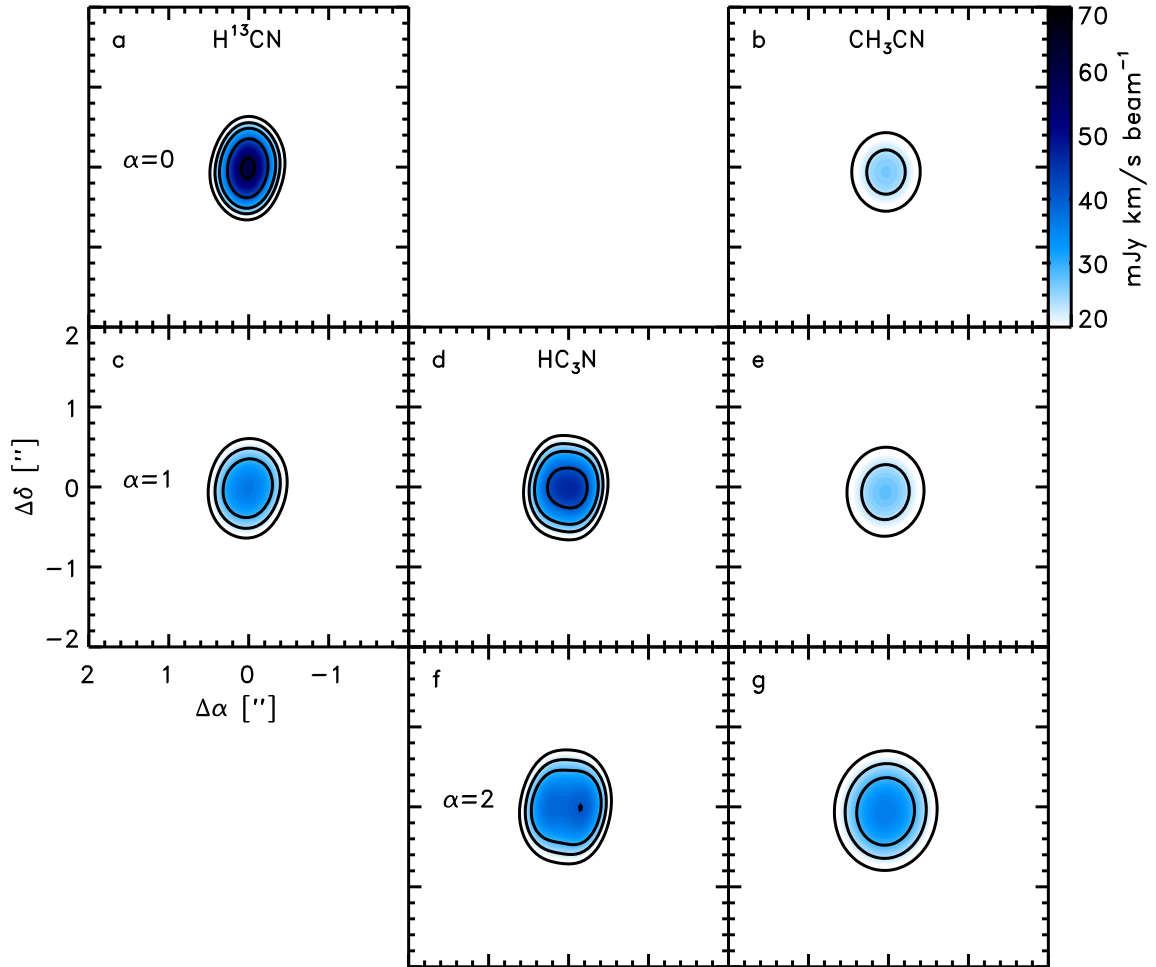
Extended Data

**Extended Data Figure 1:** Physical model for the disk of MWC 480

| Parameters	Values
Stellar properties	
Estimated distance: d (pc)	140
Stellar mass: M_* ($M_\odot$)	1.8
Disk structure properties	
Disk mass: M_d($M_\odot$)	0.18
Characteristic radius: R_c(AU)	81
Outer cut-off radius (AU)	100
Scale height: H_{100AU} (AU)	16
Flaring index: h	1.25
Density power-law index: γ	0.75
Midplane temperature: T_{100AU} (K)	23
Temperature power-law index: q	0.5
Vertical temperature gradient index: β	1.5
Disk geometric and kinematic properties	
Inclination: i (deg)	37
Systemic velocity: V_{LSR}(km s^{-1})	5.0
Turbulent line width: v_{turb}(km s^{-1})	0.05
Position angle: P.A.(deg)	58
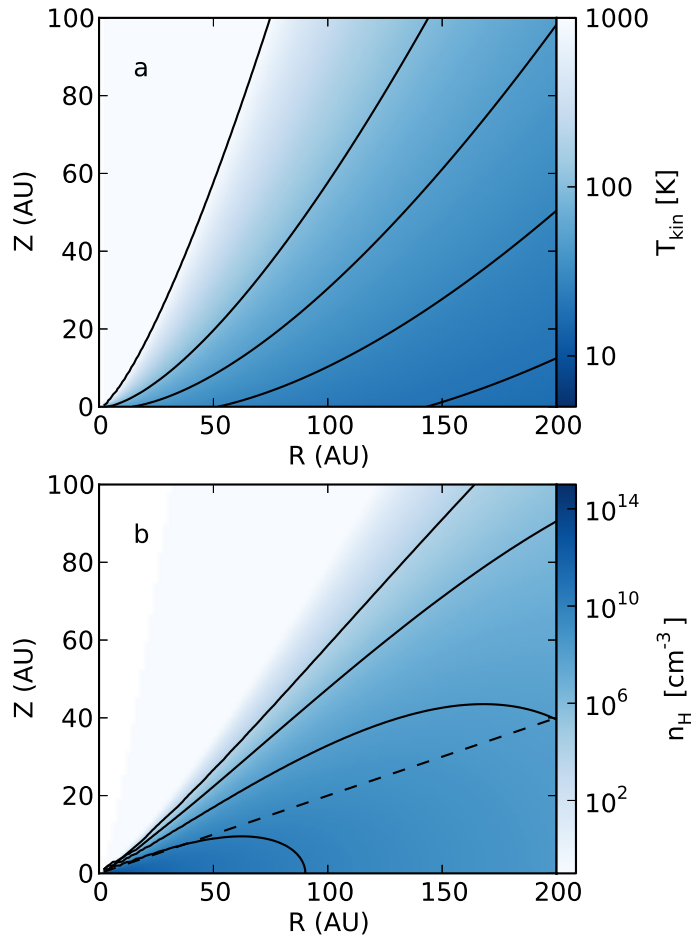
Extended Data Figure 1: Model of the physical structure of the MWC 480 proto-planetary disk. a, radial and vertical disk temperature profile (color: see color scale on the right, contours: 20,30,50,100, and 1000 K) with important temperatures marked with contours. b, radial and vertical density profile (color: see color scale on the right, contours: 10^{10}, 10^8, 10^6 and 10^4 cm^{-3}). The disk height over radius of 0.2 is marked as well.

19

Extended Data Figure 2: Synthetic observations of H^{13}CN, HC$_3$N and CH$_3$CN.
The models are based on best-fit to data for different choices of α. a–g, integrated emission
maps (colour: see colour scale on the right). Black contours are the observed $[3,4,5,7,10]\sigma$
in Fig. 1. The synthesized beam is shown in the bottom left corner of each panel. Note
the change in emission profile between $\alpha = 1$ and 2 for HC$_3$N.
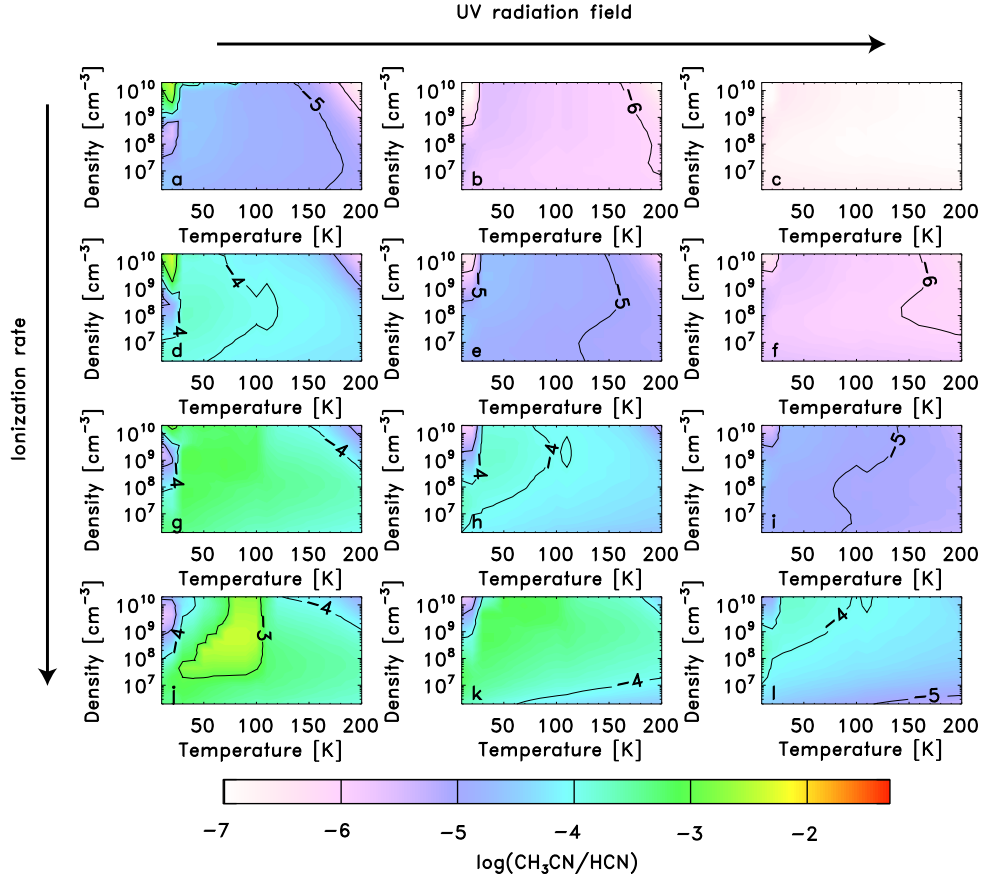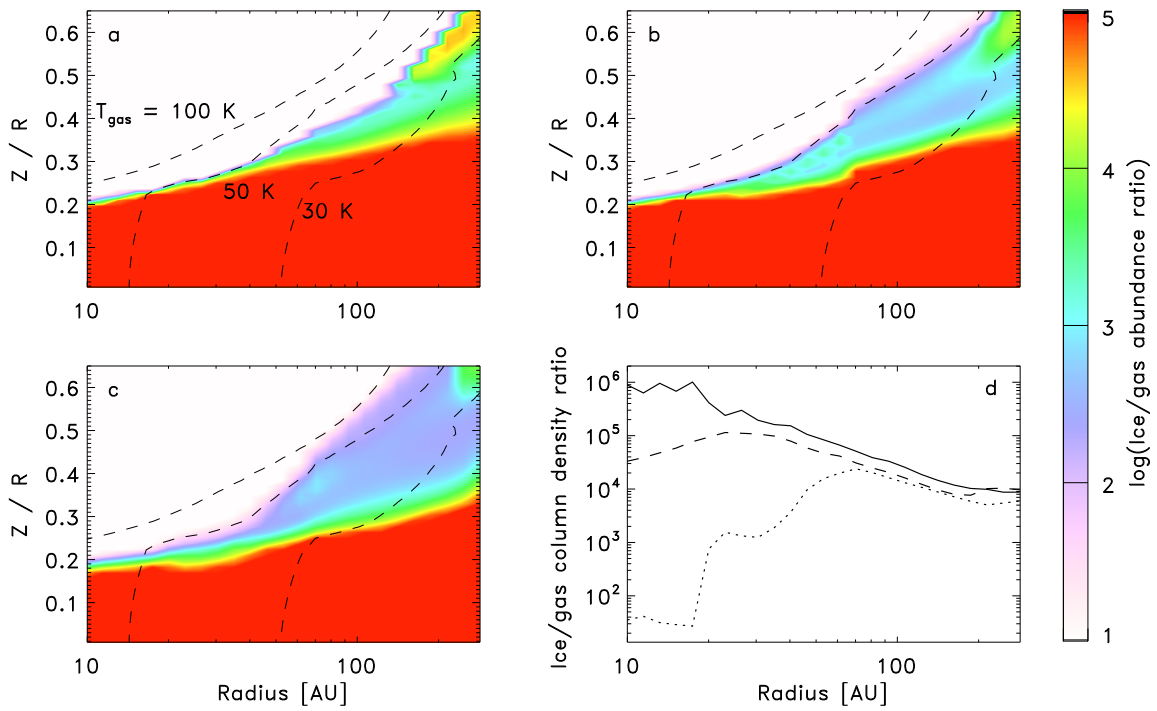
Extended Data Figure 3: Models of gaseous CH₃CN/HCN abundance ratios under different physical conditions. a–l, the CH₃CN/HCN abundance ratio on a logarithmic scale (colour: see colour scale on the bottom). UV radiation flux increases from left to right from $G_0 = 1$ (a,d,g,j) to $G_0 = 10$ (b,e,h,k) to $G_0 = 100$ (c,f,i,l), where G_0 is scaling factor in multiples of the local interstellar radiation field. The ionization rate of H_2 increases from top to bottom from 10^{-17} s^{-1} (a–c) to 10^{-16} s^{-1} (d–f) to 10^{-15} s^{-1} (g–i) to 10^{-14} s^{-1} (j–l).
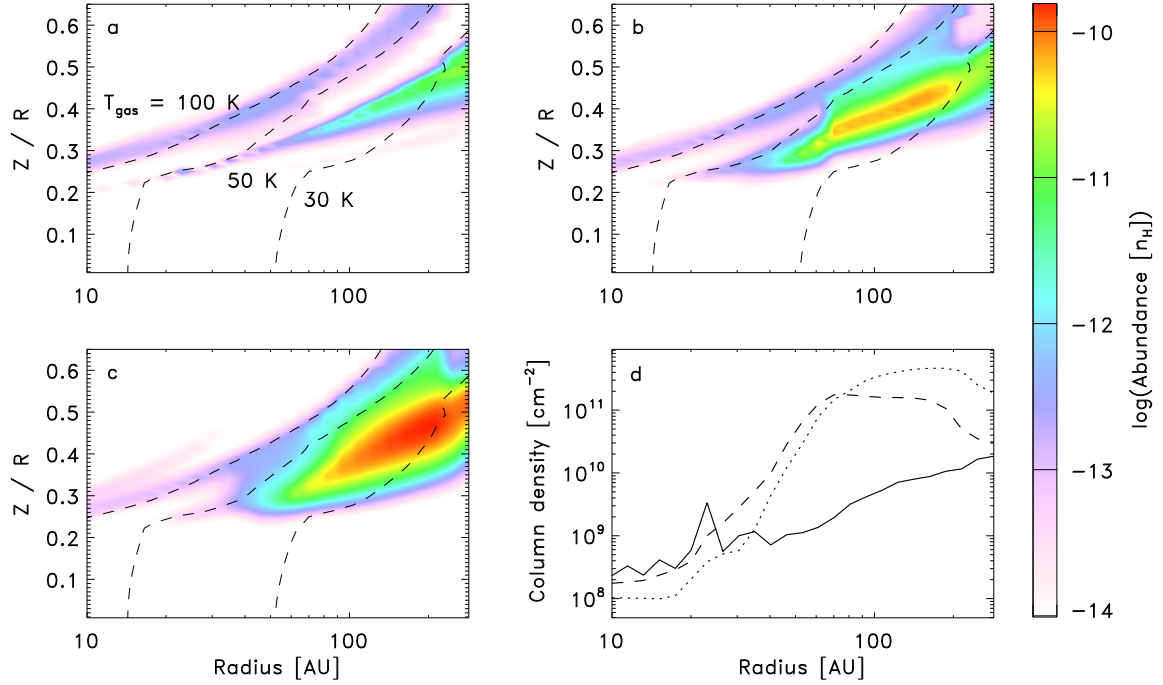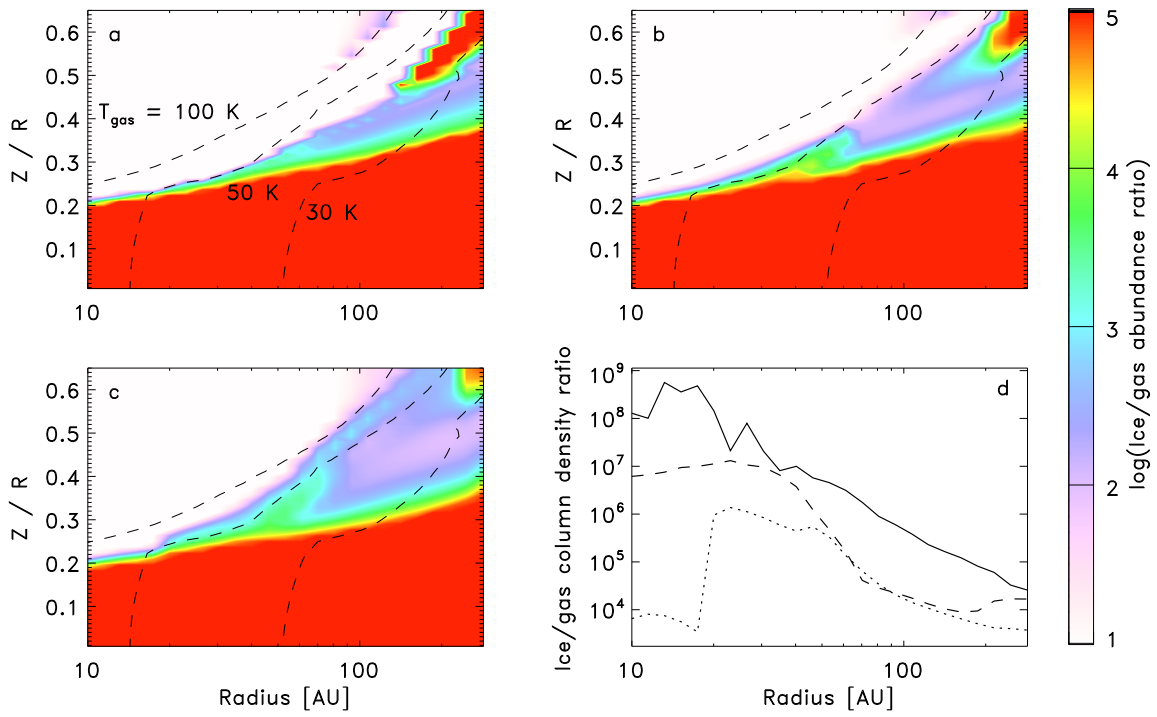
Extended Data Figure 4: Models of gaseous CH$_3$CN in disks with and without turbulent diffusion. a, the abundance of CH$_3$CN (colour: see colour scale on the right) as function of disk radius (R) and height scaled by the radius (Z/R) in a model without turbulence. The dashed lines indicate gas temperatures of [30,50,100] K. b–c as a, but in disk models that include turbulence parameterized by $\alpha_z = 10^{-3}$ (b) and $\alpha_z = 10^{-2}$ (c). d, the vertically integrated column density of CH$_3$CN from a–c (solid line: $\alpha_z = 0$, dashed line: $\alpha_z = 10^{-3}$, dotted line: $\alpha_z = 10^{-2}$).
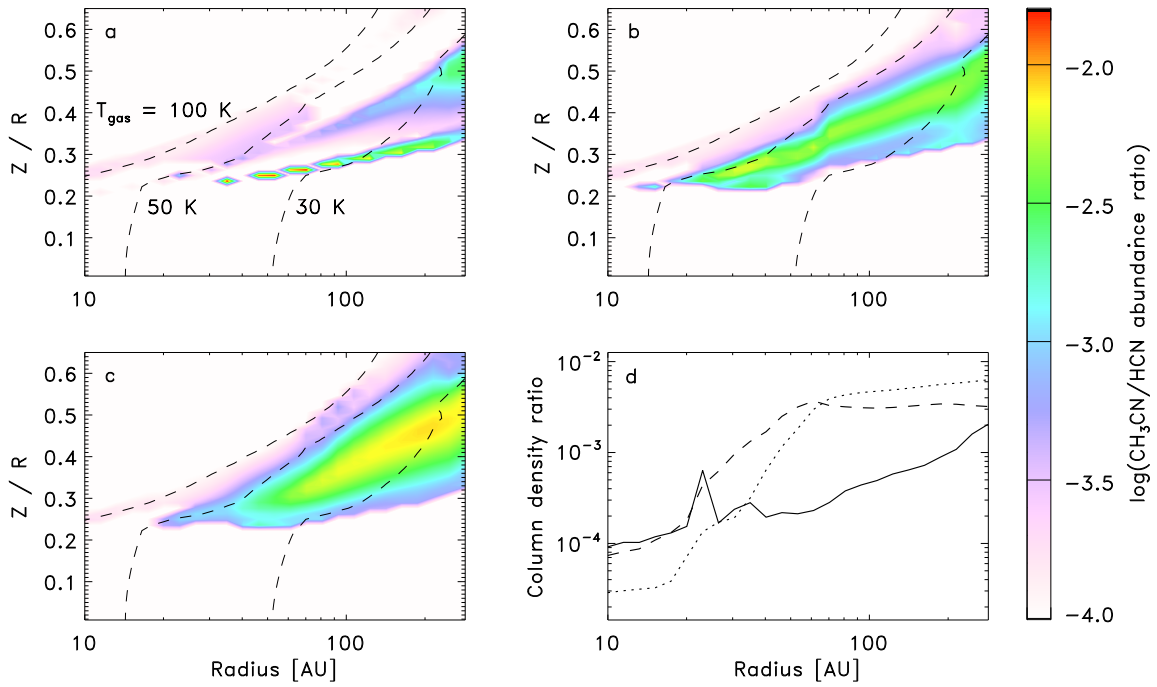
Extended Data Figure 5: Models of gaseous CH₃CN/HCN ratios in disks with and without turbulent diffusion. a–d, as in Extended Data Fig. 4.

23

Extended Data Figure 6: **Models of gas-to-ice ratios of HCN in disks with and without turbulent diffusion.** a–d, as in Extended Data Fig. 4.

Extended Data Figure 7: Models of gas-to-ice ratios of CH$_3$CN in disks with and without turbulent diffusion. a–d, as in Extended Data Fig. 4.